29 September, 2015

Limitations on fluid grid sizing for using volume-averaged fluid equations in discrete element models of fluidized beds

Christopher M. Boyce[a,c*], Daniel J. Holland[a,d], Stuart A. Scott[b], J. S. Dennis[a]

(a) Department of Chemical Engineering and Biotechnology, University of Cambridge, New Museums Site, Pembroke Street, Cambridge CB2 3RA, UK.

(b) Department of Engineering, University of Cambridge, Cambridge CB2 1PZ, UK.

(c) Department of Chemical and Biological Engineering, Princeton University

(d) Department of Chemical and Process Engineering, University of Canterbury

(*) Corresponding author. Email: cmboyce@princeton.edu. Tel: +1-646-255-4807

Abstract

Bubbling and slugging fluidization were simulated in 3D cylindrical fluidized beds using a discrete element model with computational fluid dynamics (DEM-CFD). A CFD grid was used in which the volume of all fluid cells was equal. Ninety simulations were conducted with different fluid grid cell lengths in the vertical (*dz*) and radial (*dr*) directions to determine at what fluid grid sizes, as compared to the particle diameter (d_p), the volume-averaged fluid equations broke down and the predictions became physically unrealistic. Simulations were compared with experimental results for time-averaged particle velocities as well as frequencies of pressure oscillations and bubble eruptions. The theoretical predictions matched experimental results most accurately when dz = 3-4 d_p, with physically unrealistic predictions produced from grids with lower *dz*. Within the valid range of *dz*, variations of *dr* did not have a significant effect on the results.

1. Introduction

The computational modelling of fluidized beds has become more popular in the past few decades because increases in computational power has allowed for the simulation of a variety of different processes. Discrete element modelling with computational fluid dynamics (DEM-CFD)[1,2] is a powerful technique which models the motion of individual particles, whilst the fluid is described using volume-averaged equations of motion[3]. The derivation of the volume-averaged fluid equations[3] used in DEM-CFD models requires the fluid cells to cover regions which would not change in macroscopic physical properties if the cells were slightly changed in size[4]. Thus, it is essential that the fluid cells are sufficiently small to capture mesoscopic flow features, but sufficiently large to contain several particles. However, no clear guidance exists as to the size or shape of the fluid cells required to satisfy these limits. Indeed, to the best of the authors' knowledge, Peng et al.[5] have presented the only detailed examination of the effect of cell size on simulation. In their work, a pseudo-two dimensional (2D) fluidised bed was simulated. The present paper builds on the work of Peng et al.[5] to explore the effect of the cell size in simulations of a three-dimensional (3D), cylindrical fluidised bed.

Until recently, very few DEM-CFD simulations of 3D cylindrical fluidized beds have been conducted. DEM models were originally limited to 2D rectangular beds[6–13], primarily due to difficulties constructing discrete element models of 3D cylindrical fluidized beds and the high computational demand of fully 3D simulations. However, a cylindrical configuration is most commonly used in laboratory experiments and industry. Initial efforts to extend DEM-CFD to cylindrical fluidized beds focused on using axisymmetric conditions[14], but this method was not able to capture the truly 3D motion which occurs in 3D fluidized beds. Thus, in the past few years there has been a large effort to use DEM-CFD to model directly systems with cylindrical

and more complex geometries. To do this, three main techniques have evolved: (a) use of a rectangular fluid grid with the method of immersed boundaries[15] and (b) use of an unstructured fluid grid generated by a commercial CFD package, such as ANSYS-Fluent[16] and (c) the use of a conventional 3D fluid grid in cylindrical coordinates[17]. In all three techniques, a difficulty arises because it is impossible to keep fluid cells approximately equal in volume and similar in shape, avoiding large aspect ratios in side length.

This problem of sizing fluid cells presents itself at the boundaries using the immersed boundary method. For example, in a simulation with a cylindrical wall, the rectangular fluid cells on the axis are of uniform size, yet the cells at the wall can be significantly smaller and have oblong shapes. In conventional grids using cylindrical coordinates, the fluid cells become very narrow in the angular direction near the central axis, making them oblong with a small volume. Conversely, near the radial extremities, the cells become very wide, making them oblong in the opposite direction, with a very large volume. This issue is even more apparent in unstructured grid models, where fluid cells can have a variety of shapes and vary greatly in side-length and volume. In most papers on DEM-CFD with unstructured grids, fluid cell volumes and side-lengths are not quoted; however, in one paper, the side-length of the fluid grid was quoted as 2-10 times larger than the diameter of the particle[18] with the minimum volume of a CFD cell as 4.2 mm^3, 16 times larger than that of the particles used[19]. Others[20] have used a volume for the fluid cells varying from 35 to 617 mm^3, with the smallest cell having a volume 3.05 times that of the average particle in the simulation. While the theoretical basis for the applicability of the volume-averaged fluid equations is well-documented[3,4], the practical quantitative limits are not well understood. With the order-of-magnitude differences in fluid cell side-length and volume

introduced to enable modelling of complex geometries, it is now more important to understand the limits at which these volume-averaged equations break down.

In a DEM-CFD study of pneumatic conveying through a bend in a pipe using an unstructured fluid grid, Chu and Yu[20] conducted trial simulations with finer grid meshes than those used in the results presented and did not observe any noticeable differences, thus concluding that the grid sizing used was appropriate. This approach is analogous to that used in single phase CFD where it is common to run simulations with successively finer grids to obtain a "grid independent" simulation. However, a study of a spouted bed using a 3D cylindrical fluid grid[17] reported that simulations with a fluid grid side length less than 2 particle diameters resulted in the spout collapsing owing to numerical instabilities. Similarly, Müller *et al.*[11] suggested that a grid size of approximately 3-4 times the particle diameter be used in DEM-CFD simulations to ensure the assumptions underlying the volume-averaged fluid equations would be satisfied. However, this study was conducted on a pseudo-2D rectangular fluidized bed and only two different side lengths were used in the x, y and z directions. No detailed investigation of the effect of the grid size was undertaken, making this suggestion far from conclusive. Link *et al.*[21] were able to obtain grid independent solutions for grid sizes in the range 2-4 d_p by developing a voidage calculation method that distributes the volume of a particle over a cube of side length 5 d_p. However, this grid independence was found only by comparing simulation results for a pseudo-2D spouted bed with grid sizes of 2 d_p and 4 d_p. Thus, it is difficult to assess whether this grid independence would transfer to 3D systems with different flow conditions as well as models with less spatial smoothing in calculating voidage, which are more common.

Recently, Peng *et al.*[5] have conducted a detailed study on the effect of the size of the fluid grid in a pseudo-2D fluidised bed and concluded the following: (1) When using fluid grid cells

with side-lengths (S_c) less than 3.82 particle diameters (d_p) (i.e. $S_c < 3.82\ d_p$), the particle centroid method (PCM) for calculating voidage does not give physically realistic results. (2) If a characteristic length for the size of the simulation domain (S_d) is less than 19.3 times larger than the cell size (i.e. $S_d < 19.3\ S_c$), the fluid grid is too coarse to capture mesoscale flow structures necessary for physically accurate simulation predictions. (3) When $S_c < 1.63\ d_p$, simulations become physically unrealistic because the cells are too small to satisfy the assumptions made in the derivation of the volume-averaged fluid equations. These findings provide the first detailed analysis of the minimum and maximum fluid grid size that should be used when performing DEM-CFD simulations.

However, the conclusions of Peng *et al.*[5] require further investigation. Their simulations were of a pseudo-2D fluidized bed where wall effects will dominate. In fully 3D fluidised beds, wall effects will be less significant. Also, Peng *et al.*[5] characterised the domain size and the fluid grid spacing using either the volume of the entire simulation domain or that of an individual cell, respectively ($S_d = \sqrt[3]{V_{domain}}; S_c = \sqrt[3]{V_{cell}}$). It is unclear as to how much freedom there is to vary the linear dimensions of the cell within the given volume. Lastly, the simulations were compared with experimental results for pressure fluctuations and bubbling characteristics qualitatively; further quantitative validation of additional simulation predictions is needed. Thus, the literature is still in need of studies which systematically investigate the proper range of fluid grid sizes for use in fully 3D DEM-CFD simulations.

The present paper builds on the work of Peng *et al.*[5], addressing the issues raised in the preceding paragraph. To investigate the range of fluid grid sizes for which the volume-averaged equations remain accurate and valid in non-rectangular fluid grids, the present work utilised a 3D cylindrical DEM-CFD model in which all fluid cells were equal in volume and similar in shape.

2. Methods

A 3-D, cylindrical, discrete element model with computational fluid dynamics (DEM-CFD), described fully elsewhere[22], was used to simulate bubbling fluidization in three different bed configurations: (1) a bed with diameter D_{bed} = 44 mm and settled bed height H_0 = 30 mm, (2) a bed with D_{bed} = 50 mm and H_0 = 40 mm and (3) a bed with D_{bed} = 50 mm and H_0 = 50 mm. The model[22] has been validated experimentally for time-averaged particle velocity[23] and the frequency of pressure oscillations and bubble eruptions in bubbling fluidized beds[24].

In brief, the model tracks the position of each particle in rectangular coordinates, while enclosing the particles in cylindrical walls. The flow of gas was calculated using a special geometry of cylindrical fluid grid[22]. Particle contacts were modelled using a soft-sphere approach, with a Hertzian spring and dashpot model in the normal direction and the model of Tsuji *et al.*[25] used in the tangential direction, with Coulomb's law introduced to account for sliding. The fluid and particle equations were stepped forward in time using the fully-explicit, 3rd order Adams-Bashforth method, so as to allow pressure waves to travel through the system. At the inlet to the bed, fluid velocities were specified, with the vertical fluid velocity ramped from zero at initialisation to the desired inlet velocity and the velocities in the radial and angular directions set to zero. In all three bed configurations, the distributor at the inlet was modelled as a porous plate, with even distribution of gas. A characteristic outlet boundary condition suitable for 3D cylindrical geometry[26] was employed, as described elsewhere[22], to allow pressure waves to exit the system. Full-slip boundary conditions were imposed on the fluid at the walls, as it was not expected that the fluid grids used, especially those with coarser fluid grids in the radial direction, would be able to capture the boundary layer of no-slip boundary conditions properly[11].

In using a discretised 3D cylindrical grid, the radial fluid velocity (u_r) needed to be interpolated along the central ($r = 0$) axis in order to discretise the fluid equations properly and avoid creating a physical boundary along this axis. The radial velocity was interpolated along the axis using a single-value scheme similar to that used by Takeuchi *et al.*[17] and Fukagata and Kasagi[27], and described in Appendix A.

The fluid and particle interaction was accounted for (1) in the calculation of voidage for each fluid control volume and (2) in the fluid-particle interaction force. Void fraction was calculated on the cylindrical grid using the "square grid method" described in full elsewhere[22]. Effectively, the method calculates the distribution of particle volume on a square grid with side length slightly larger than the particle diameter (d_p = 1.2 mm; square grid side-length: 1.3 mm). If a particle lies in multiple square grid cells, its volume is divided between these cells by approximating the spherical particle as a cube with side-length equal to the particle diameter, and calculating the fraction of the volume of the cube in each square grid cell[28]. This calculation is the same as that presented by Link et al.[21], except Link et al.[21] approximated the volume of the particle as a cube with side length of 5 d_p in order to smooth the particle volume over several grid cells. In the "square grid method" used here, the distribution of particle volume is then translated to the cylindrical fluid grid cells, based on the fraction of volume of the square grid cells which lies in the cylindrical grid cells. The void fraction in the cylindrical fluid grid cells is then calculated based on the total particle volume assigned to each cylindrical grid cell. The force of interaction between the fluid and particles was modelled using the drag law of Beetstra *et al.*[29], because Müller *et al.*[11], using a rectangular version of the present program, found it matched experimental results better than other common drag laws used in DEM-CFD modelling. For these calculations, the gas velocity used for the drag on a particle was taken from the grid

cell in which the particle was centred, and the drag on the fluid was assigned entirely to that same grid cell.

The cylindrical grid was such that, whilst the spacing of fluid cells in the radial and vertical directions was constant, more fluid cells were used in the outer annuli than the inner annuli, such that the volume of all fluid cells was held constant. An example of a horizontal cross section of a fluid grid in which 5 fluid cells are used in the radial direction is shown in Figure 1; the numbers on the grid count the number of fluid cells used in each annulus. The spacing of fluid cells in the radial and vertical directions (*dr* and *dz*) for bed configuration 1 was varied systematically from *dr* = 2.75 mm to 5.50 mm and *dz* = 2.4 mm to 7.2 mm to investigate the effect of grid size on the predictions of the simulation. In all cases for bed configuration 1, the overall dimensions of the boundaries of the fluid grid were kept constant, being, overall, 44 mm in diameter and 116 mm in height. Since the number of fluid cells in each annulus increases with fluid grid size, the sizing of cells in the angular direction also decreases with decreasing *dr*. Figure 2 shows horizontal cross sections of fluid grids with the largest horizontal grid sizing used (*dr* = 5.50 mm) and the smallest horizontal grid sizing used (*dr* = 2.75 mm) to demonstrate this difference. For bed configurations 2 and 3, *dr* was varied from 2.5 to 6.25 mm and *dz* was varied from 2.4 to 6.0 mm, while the overall dimensions of the fluid grid were kept constant at 50 mm in diameter and 204 mm in height.

Simulations of 2.1 s of steady bubbling fluidization, after a 0.7 s period of start-up, were conducted for each size of fluid grid and each bed configuration. The particles simulated were spherical, 1.2 mm in diameter, with a particle density of 900 kg/m^3 in bed configuration 1 and 960 kg/m^3 in bed configurations 2 and 3. The minimum fluidization velocity for these particles, determined experimentally, was U_{mf} = 0.3 m/s and the bed was fluidized at $U = 2U_{mf}$ for bed

configuration 1 and $U = 1.88U_{mf}$ for configurations 2 and 3. Details of the parameters used, including those for contact mechanics, are summarised in Table 1. For each simulation in bed configuration 1, the following were determined: (1) the time-averaged particle velocity over the 2.1 s of steady bubbling for particles located in a vertical slice in the centre of the bed, 5 mm in depth and (2) a representative map of instantaneous particle void fraction in a vertical slice in the centre of the bed, 5 mm in depth, as a bubble approached the bed surface. Time-averaged particle velocity was calculated based on the number of particles which passed through a voxel, with the velocity of each particle receiving equal weighting towards the ultimate average. This method of averaging was determined to be equivalent to that used in magnetic resonance imaging (MRI)[23].

For bed configurations 2 and 3, the frequency of pressure oscillations 10 mm above the distributor as well as the frequency of bubble eruptions at the bed surface were determined from the maxima in the power density spectra of pressure and void fraction, respectively, as described by Boyce *et al.*[24]. The frequency of bubble formation was also determined based on the power density spectra of the void fraction 10 mm above the distributor. Additionally, representative maps of the instantaneous voidage as a bubble approached the bed surface were taken from a 5 mm vertical slice in the centre of the bed for configurations 2 and 3.

The theoretical predictions of the behaviour of bed configuration 1 were compared with the experimental results of Holland *et al.*[30], who used MRI to measure time-averaged particle velocity for particles in a 5 mm vertical slice in the centre of a bubbling fluidized bed. The bed dimensions, particles and superficial gas velocity (U) used by Holland *et al.*[30] were the same as those simulated using DEM-CFD, except that the experimental particles were non-spherical, with a "comma-like" shape[30].

For a quantitative comparison between the profiles of time-averaged particle velocity predicted by the DEM-CFD with various grid sizes and the experimental results, the deviation of the velocities predicted and those measured was evaluated. To do this, the squared difference in vertical velocity in each pixel was calculated. The size of each pixel was 1.04 mm (z) by 0.94 mm (x) by 5.0 mm (y) to match that measured experimentally by Holland *et al.*[30]. The squared differences were then summed for all pixels up to 42 mm above the distributor to obtain the overall mean squared deviation in velocity ($(\Delta v)_{tot}^2$), according to:

$$(\Delta v)_{tot}^2 = \frac{\sum_{i=1}^{N_{pixels}} \left(V_{z,DEM}(i) - V_{z,MRI}(i)\right)^2}{N_{pixels}} \qquad (1)$$

where $V_{z,DEM}(i)$ and $V_{z,MRI}(i)$ are the time-averaged particle velocities predicted by DEM-CFD and measured using MRI, respectively, in pixel i and N_{pixels} is the total number of pixels up to 42 mm above the distributor. A height of 42 mm was chosen so as to have as complete a comparison as possible between experimental and computational results, whilst being well below the top surface of the bed and not significantly influenced by differences in expanded bed height between experimental results and all computational predictions[23].

For a second quantitative comparison between the profiles of time-averaged particle velocity, the magnitudes of the fastest moving upward and downward sections of the velocity profiles were determined. The velocities from the pixels with the highest 10% of average velocities were averaged for each simulation to produce a representative value for the upward moving velocity profile. Similarly, the velocities from the pixels with the lowest 10% (most negative) of average velocities were averaged to produce a representative value for the downward moving velocity profile. These values were compared with those from the experiments.

The simulations for bed configurations 2 and 3 were compared with the experimental results of Müller *et al.*[31], who measured (i) the frequency of pressure oscillations 10 mm above the distributor and (ii) the frequency of bubble passage at the surface of the bed to measure frequency of bubble eruption there. In observing bubbles using MRI, they found that slugging occurred in bed configuration 3, but not bed configuration 2. All aspects of the simulations matched the experimental conditions, except that the particles simulated were spherical, rather than comma-shaped as in the experiments.

3. Results and Discussion

3.1 Time-averaged particle velocity

3.1.1 DEM-CFD predictions and MRI results

Figure 3 shows the time-averaged particle velocities in the vertical direction (V_z) predicted by (a) DEM-CFD simulations with varying sizes of fluid grid cells as compared with (b) the time-averaged particle velocities measured experimentally by Müller *et al.*[30]. Table 2 shows the overall squared deviation in velocity ($(\Delta v)_{tot}^2$) of each of the DEM-CFD simulations from the MRI measurements. In Figure 3, the group of velocity profiles bounded by a yellow dashed line denote those with $(\Delta v)_{tot}^2 < 0.0080$ m^2/s^2, demarcating the 10 simulations of the 30 total which match the experimental results most closely.

In all cases of fluid grids with different cell sizes, the velocity profile predicted generally matches qualitatively that measured experimentally, with an upward moving profile in the centre and a downward moving profile along the walls. However, the region of high-velocity, upward moving particles predicted by DEM-CFD simulations does not extend to the same height as that measured experimentally. Additionally, the maximum upward time-averaged velocity measured experimentally was higher than that predicted by the simulations, and the greatest downward

velocity measured experimentally, seen at the top of the expanded bed near the walls, was less negative than that predicted by the simulations. To quantify these differences in the upward and downward moving profiles, Tables 3 and 4 show the average velocities from the 10% of pixels with the highest and lowest velocities, respectively, for the simulations with varying grid sizes. The experimental results for the average velocity in the pixels with the highest 10% of velocities was 0.410 m/s, significantly higher than that seen in the simulations, and the average velocity in the pixels with the lowest 10% of velocities was -0.180 m/s, significantly lower (more negative) than in the simulations. Thus, three criteria can be viewed as characteristic of simulations predictions which match the experimental results most closely: (1) a uniform upward moving profile in the centre, extending to the surface of the bed, (2) a high maximum time-averaged velocity in the centre of the upward moving profile and (3) a time-averaged downward moving velocity large in magnitude near the walls at the top of the expanded bed.

Figure 3a shows systematic differences in the time-averaged velocity profiles predicted by the DEM-CFD simulations with different sizes of fluid cells. In the first two columns, with *dz* = 2.4 mm and 3.0 mm, the upward moving profiles are generally shifted to the right, and tilted upwards to the right at the top of the expanded bed. This shifting and tilting is less pronounced with increasing radial spacing, *dr*; in the case of *dr* = 5.5 mm, the rightward shifting and tilting is no longer seen, but the upward moving profiles are narrow and pointed at the top. In all cases, for *dz* = 2.4 and 3.0 mm, the magnitudes of the velocities in the upward moving profile are noticeably lower than those seen in profiles for simulations with larger *dz*, as demonstrated in Table 3. The simulation with *dz* = 3.0 mm and *dr* = 3.14 mm produced a velocity map with $(\Delta v)_{tot}^2 < 0.0080$ m^2/s^2; however, the tilting of the predicted velocity profile near the top is qualitatively different from that seen experimentally.

In the third and fourth columns of Figure 3, with *dz* = 3.6 and 4.8 mm, the upward moving profile is central and rounded at the top. The velocities seen in the time-averaged upward moving profile are generally the greatest for these fluid grid sizes, as shown in Table 3. Additionally, the downward velocities at the top of the expanded bed near the walls are also generally the greatest in magnitude, as shown in Table 4. Thus, the predictions for time-averaged particle velocity provided by DEM-CFD with vertical fluid grid spacing *dz* = 3.6 and 4.8 mm match the experimental results most closely. No major differences can be seen by varying radial grid spacing, *dr*, for this range of *dz*; however, simulations with *dr* = 5.50 mm were the ones in this range of vertical spacing which did not have $(\Delta v)_{tot}^2 < 0.0080$ m^2/s^2.

In the fifth and sixth columns of Figure 3, with *dz* = 6.0 and 7.2 mm, the upward moving flow profile remains central, but is shorter and generally has a lower maximum upward velocity, as compared to fluid grids with *dz* = 3.6 and 4.8 mm. Additionally, for *dz* = 6.0 and 7.2 mm, the time-averaged downward velocity near the walls at the top of the expanded bed is very close to zero, and does not match the pronounced downward velocity seen experimentally in this region. For *dz* = 6.0 and 7.2 mm, there is not much difference in the time-averaged velocity profile predicted with varying *dr*. The simulation with *dz* = 6.0 mm and *dr* = 3.67 mm was the only one which produced a velocity map with $(\Delta v)_{tot}^2 < 0.0080$ m^2/s^2 in this range of vertical spacing. However, the differences between the velocity map predicted for this grid sizing and those predicted by the other simulations in this range of vertical spacing are not obvious.

3.1.2 Reasoning for quantitative differences between simulations and experimental results

As noted in Section 3.1.1, none of the predictions for time-averaged particle velocity by the various DEM-CFD simulations completely matches the experimental results of Müller *et al.*[30]. The most notable differences in the DEM-CFD predictions, compared with experiment, are

(1) the region of upward moving high-velocity particles is shorter, (2) the maximum time-averaged upward velocity is lower, and (3) the maximum time-averaged downward velocity, located at the top of the expanded bed at the walls, is also lower in magnitude. As detailed in Boyce *et al.*[23], these differences can be attributed to deficiencies in simulating the drag force on the particles exerted by the fluidizing gas. These deficiencies come from (a) the fact that the simulated particles are spherical and (b) the use of the drag law of Beetstra *et al.*[29], which has been shown to underestimate drag in fluidized beds[32].

The fact that the simulated particles are spherical, while the particles used experimentally are comma-shaped, means that the simulated particles will have less surface area for the fluidizing gas to lift them up, potentially explaining the lower expanded bed height and lower maximum upward particle velocity. The underestimation of the drag force by the drag law used can also explain these two differences. Part of the reason the Beetstra *et al.*[29] drag law might underestimate drag force comes from the fact that it is based on a series of lattice-Boltzmann simulations in which particles were randomly dispersed in a unit cell, but all moved through the fluid in the same direction at the same velocity. Thus, the drag law developed does not account for the motion in varying directions which can occur in bubbling fluidized beds, and therefore Kriebitzsch *et al.*[32] have recommended the development of a similar drag law which takes granular temperature into account. As noted earlier, the drag law of Beetstra *et al.*[29] was nevertheless used because it was shown to give simulated results which most closely matched experimental evidence in a previous study[11]. The regions of largest downward particle velocity arise from particles falling downwards near the walls of the bed after being ejected into the freeboard upon bubble eruption. These downward velocities will be lower in magnitude if the particles are ejected into the freeboard with a lower upward velocity. Thus, the deficiencies in

simulating drag also account for this third main difference seen in the DEM-CFD simulations *versus* experimental results.

In future studies, different measures could be taken to try to improve the accuracy of the simulation predictions. First, a drag law which accounts for the particles being non-spherical could be used[33,34]. Also, other interaction forces could be accounted for, such as the Magnus lift force. Additionally, a coarse-grained drag force model, such as that proposed recently by Radl and Sundaresan[35] could be used to see if it improves simulation accuracy, especially in larger fluid grids; however, since such a drag model is expected to be of more impact in situations where the grid spacing is greater than 10 d_p, using a filtered drag model is not expected to have a significant impact. These measures in modelling the interaction force were not taken in the study presented here because they are not commonly used in DEM-CFD modelling today.

3.1.3 DEM-CFD predictions of particle distribution in bed configuration 1

To understand how the differences in maps of time-averaged particle velocity arise as a function of size of grid, instantaneous maps of voidage (ε) showing bubbles approaching the surface of the bed are given in Figure 4. In these images, black indicates regions with a very low density of particles, while white indicates regions with a high density of particles. These images show the distribution of particles in a 5 mm central slice of the bed in the vertical direction. In Figure 4, the group of voidage maps bounded by a red dashed line denote those coming from simulations with $(\Delta v)_{tot}^2 < 0.0080$ m^2/s^2.

In the first column in Figure 4, for simulations with fluid cells with *dz* = 2.4 mm and *dr* = 2.75, 3.14 and 3.67 mm, the bubble extends diagonally from bottom left to top right, with a line of particles dividing it across the centre. For simulations with *dz* = 2.4 mm and *dr* = 4.40 and 5.50 mm, the bubble is horizontally symmetric, yet shorter vertically than those predicted by

simulations with larger $dz > 3.0$ mm. These trends are generally seen in the second column, where $dz = 3.0$ mm, except in the case of $dr = 5.50$ mm, which gives a very similar bubble shape to that from the simulation with $dz = 2.4$ mm and $dr = 5.50$ mm, and in the case of $dr = 4.40$ mm, in which the bubble is slightly horizontally biased from bottom left to top right.

In the case of $dz = 3.6$ and 4.8 mm, the bubbles are generally large and horizontally symmetric, spanning the majority of the bed diameter; the bubbles are not spherical, but rather have a dimpled bottom, characteristic of having a wake of particles entrained below them. For these vertical fluid grid sizes ($dz = 3.6$ and 4.8 mm) little systematic difference is seen in bubble shape with varying radial grid spacing (dr).

Similar to simulations with $dz = 3.6$ and 4.8 mm, simulations with $dz = 6.0$ and 7.2 mm show large bubbles which are horizontally symmetric. However, the dome of particles pushed to the top of the bed by these bubbles tends to be flatter in simulations where $dz = 6.0$ and 7.2 mm, and a small amount of bridging occurs, where the bubble spans the entire diameter of the bed near its bottom. The width of the bubbles changes for the different grid spacings. The bubbles in the $dz = 6.0$ and 7.2 mm simulations become progressively narrower from the base of the bubble to the tip, and thus have an approximately conical shape. The bubbles in the $dz = 3.6$ and 4.8 mm simulations are of almost constant width above the wake region with the bubble only narrowing towards the nose; thus these bubbles have an almost cylindrical shape with a rounded nose. The shape of the wake of the bubbles for simulations with $dz \geq 3.6$ mm is approximately the same. These differences in the shape of bubbles correspond to differences in the time-averaged velocity profiles, as discussed in Section 3.1.4.

3.1.4 Effect of fluid grid sizing on time-averaged particle velocity predictions

The DEM-CFD predictions shown in Figures 3 and 4 suggest that varying the height of the fluid grid in the vertical direction (*dz*) has a greater impact on the predictions than a commensurate change in the radial dimension (*dr*). Specifically, the tilted and split nature of the bubbles seen for simulations with *dz* = 2.4 and 3.0 mm demonstrates non-physical behaviour simulated when *dz* < 3.6 mm. Increasing *dr* when *dz* is small seems to make the predictions closer to the experimental observations, as shown by the fact that the bubbles simulated in the cases of *dr* = 5.50 mm and *dz* = 2.4 and 3.0 mm are central horizontally and no longer divided by a line of particles. However, these bubbles are still squatter than those simulated using a higher *dz*, and all simulations with *dz* < 3.6 mm predict time-averaged velocity profiles which are furthest from those found experimentally. The right-tilted nature of the upper regions of the upward moving velocity profiles in many of the time-averaged velocity profiles for simulations with *dz* < 3.6 mm derives from the fact that bubbles rising to the bed surface are tilted to the right.

A distinct difference is seen for simulations in which *dz* = 3.6 and 4.8 mm. These simulations all show large, horizontally-central bubbles, and have time-averaged velocity profiles which most closely match experimental results. The upward moving particle velocity profiles are tall and horizontally-central for these simulations since the bubbles simulated are tall and rise through the centre of the bed. The predictions of simulations with these values of *dz* do not change much when *dr* is varied between 2.75 and 5.50 mm, stressing that variance of *dz* has a greater impact on simulation predictions than variance of *dr*. However, the velocity profiles have a total squared deviation from experiment, $(\Delta v)_{tot}^2 > 0.0080$ m^2/s^2 when *dr* = 5.50 mm in this range of vertical spacing. This finding indicates that there is an upper bound on radial

spacing above which finer fluid flow patterns can no longer be captured, and hence the physical phenomena are not predicted with a high level of accuracy.

The DEM-CFD simulations with $dz > 4.8$ mm are closer to those from simulations with $dz = 3.6$ and 4.8 mm than the predictions from simulations with $dz < 3.6$ mm; however, there are subtle differences. For simulations with $dz > 4.8$ mm, the upward velocity profile is slightly squatter and the region highest in velocity is smaller area-wise; these differences are most apparent for simulations with $dz = 7.2$ mm. The differences in the velocity profile seem to come from the fact that the bubbles show more bridging and do not create as high a dome of particles as they reach the upper surface of the bed. The differences at high values of dz are smaller than those at low values of dz, and the simulations still seem physically sensible, demonstrating that it can be more difficult to notice inaccuracies in simulations due to fluid grids which are too coarse. This greater difficulty in noticing inaccuracies in fluid grids which are too coarse rather than too fine can be attributed to the fact that the volume averaged fluid equations can break down in fluid grids which are too fine, while the assumptions underlying the equations should still be satisfied in coarse grids. Differences in predictions for simulations with coarse grids probably come from subtle differences in fluid flow not detected in coarse grids.

To summarise, the results in Figures 3 and 4 demonstrate that the violation of the assumptions of the fluid averaging equations which comes with using fluid cells which are too small leads to errors in the time averaged velocity distribution. These errors are related to the prediction of non-physical bubble shapes and are more significant than errors related to the coarse graining of the fluid flow field which may arise from using large fluid cells. In these simulations, fluid cell sizes with $dz < 3\ d_p$ were found to be too small, while cells with $dz > 4\ d_p$

were too large. The simulations were not very sensitive to changes in the radial length of the fluid cells, at least not within the range 2 $d_p < dr < 5\ d_p$.

3.2 Frequencies of pressure oscillations and bubble eruption

3.2.1 DEM-CFD predictions and experimental results

Figure 5 shows DEM-CFD predictions of frequencies of (a) pressure oscillations 10 mm above the distributor and (b) bubble eruption at the bed surface for simulations with varying fluid grid sizing, compared with experimental results[31] for bed configuration 3. The corresponding results for bed configuration 2 lead to the same conclusions and are not included here for brevity; these results are shown in Appendix B. In Figure 5, for the bed with H_0 = 50 mm, the predicted frequencies of pressure oscillations and bubble eruptions increase only slightly with increasing *dr*, but change more significantly with varying *dz*. The frequencies steadily decrease with increasing *dz* in the range of *dz* = 2.4-4.8 mm, but the frequencies dramatically increase for *dz* = 6.0 mm. The frequencies measured experimentally are less than those predicted by the simulations, but simulations with *dz* = 4.8 mm provide the closest match with experimental results. The simulation with *dz* = 2.4 mm and *dr* = 3.13 mm is an outlier which predicts frequencies of bubble eruption and pressure oscillations much higher than all of the other simulations, and thus further from experimental results.

Figure 6 was constructed to see how the predictions compared to two key findings of the experimental study[31] of pressure oscillations and bubble eruption that (1) the frequency of pressure oscillations near the distributor is always approximately equal to the frequency of bubble eruption at the bed surface, (2) the frequency of pressure oscillations and bubble eruption decreases dramatically as settled bed height increases from 40 to 50 mm. The plots in Figure 6 (a) and (b) show the ratio of the frequency of pressure oscillations to that of bubble eruption for

the beds with H_0 = 40 mm and 50 mm, respectively. These results indicate that nearly all the grid configurations predict the frequencies of bubble eruption and pressure oscillations to be equal for settled bed heights of 40 and 50 mm, as was seen in the experimental results. The only exceptions were simulations with dz = 3.0 mm and dr = 2.5-4.17 mm for H_0 = 40 mm and a simulation with dz = 4.8 mm and dr = 6.25 mm for H_0 = 50 mm, all of which predict the frequency of pressure oscillations to be half that of bubble eruptions.

Figure 6 (c) shows the ratio of frequency of pressure oscillations in the 40 mm bed to that in the 50 mm bed; Figure 6 (d) shows the frequency of bubble eruptions. These results indicate that only a small set of the grid configurations properly predict the dramatic decrease in the frequencies of pressure oscillations and bubble eruption which occurs with the increase in H_0 from 40 mm to 50 mm. Only predictions with dz = 3.6 and 4.8 mm predict that the frequencies of both pressure oscillations and bubble eruption for H_0 = 50 mm are roughly half of the value of the corresponding frequencies for H_0 = 40 mm. For this range of dz, radial grid spacing, dr, does not have much effect on the simulation predictions, with nearly all of the simulations closely matching the experimental findings. The one exception in this range of dz is the simulation with dz = 4.8 mm and dr = 6.25 mm. Simulations outside this range of dz generally predicted that the frequency of bubble eruptions and pressure oscillations did not change with the increase of H_0 from 40 to 50 mm, failing to predict the second key finding of the experimental study. The only exceptions in these ranges of dz are those with dz = 3.0 mm and dr = 2.5-4.17 mm, which all failed to predict the first finding of the experimental study.

3.2.2 DEM-CFD predictions of bubbling patterns

Figures 7 and 8 show images of instantaneous particle distribution, similar to those shown in Figure 4, for simulations with varying grid sizes for bed configurations 2 and 3,

respectively. These images also come from a 5 mm central slice in the vertical direction and show a bubble as it is reaching the bed surface. They have a resolution of 2.5 mm (z) by 2.5 mm (x). The field of view is 70 mm (z) by 50 mm (x) in Figure 7 and 80 mm (z) by 50 mm (x) in Figure 8. These figures were constructed to shed light on how predicted bubble dynamics affect the frequencies of bubble eruption and pressure oscillations shown in Figures 5 and 6. The bubbles and slugs (very large bubbles) reaching the surface in Figures 7 and 8 are generally axially symmetric. Two main bubbling situations are seen in Figures 7 and 8: (A) a large slug is trailed by a small bubble in its wake and (B) a smaller slug or large bubble reaches the surface, with the next bubble only beginning to form at the distributor. These bubbling configurations have a strong tie to the second key finding of the experimental study mentioned in Section 3.2.1, as discussed in Section 3.2.3.

For the bed with H_0 = 40 mm in Figure 7, all the simulations with dz = 2.4 exhibit bubbling pattern A. For simulations with dz = 3.0 mm, those with dr = 6.25 and 5.00 mm exhibit bubbling pattern A, while those with dr = 2.50, 3.57 and 4.14 mm exhibit bubbling pattern B. The simulation with dz = 3.0 mm and dr = 3.13 mm gives a bubbling pattern somewhere in between descriptions A and B. Simulations with dz > 3.0 mm all exhibit bubbling pattern B, with the size of the bubble generally becoming larger with increasing dz and decreasing dr.

For the bed with H_0 = 50 mm in Figure 8, almost all simulations with dz < 6.0 mm exhibit some form of bubbling pattern A. The two exceptions are the simulation with dz = 2.4 mm and dr = 3.13 mm and the simulation with dz = 4.8 mm and dr = 6.25 mm, which have bubbling patterns in between patterns A and B. Simulations with dz = 6.0 mm all exhibit bubbling configuration B.

3.2.3 Effect of fluid grid sizing on pressure oscillations and bubble eruptions

As noted earlier, Müller *et al.*[31] concluded that (a) pressure oscillations at all positions in the bed are linked to bubble eruption at the surface of the bed and (b) the onset of slugging (seen in beds 50 mm or taller) leads to a dramatic decrease in the frequency of pressure oscillations and bubble eruption. Computationally, Boyce *et al.*[24] have shown that bubbles formed and erupted without interacting in the 40 mm tall bed, causing the frequencies of both bubble eruption and pressure oscillations to equal those of bubble formation. This situation is described as bubbling pattern B in Section 3.1.2. However, with the formation of slugs in the 50 mm bed, it was found[24] that a slug would interact with, and influence, the rise of one smaller bubble trailing the slug. This slug-bubble interaction caused the frequencies of bubble eruption and pressure oscillations to become half that of bubble formation, thus explaining the dramatic decrease in frequencies seen at H_0 = 50 mm. This situation is described as bubbling pattern A in section 3.2.2.

Figure 6 compares the simulations with the experimental findings, and Figures 7 and 8 show how these results relate to the bubbling patterns. Figure 6 strongly indicates that simulations with dz = 3.6-4.8 mm give the best predictions for matching experimental results, because only simulations in this range of dz give predictions in line with the two key experimental findings, observations (1) and (2) above. Figures 7 and 8 show simulations with this range of dz exhibiting bubbling pattern B for the H_0 = 40 mm bed and bubbling pattern A for the H_0 = 50 mm bed. This is in line with Boyce *et al*.[24], which showed that the transition from bubbling pattern B to pattern A caused the dramatic decrease in oscillation frequencies. The simulation with dz = 4.8 mm and dr = 6.25 mm does not agree with experiment because it does not fully exhibit bubbling pattern A in the H_0 = 50 mm bed. This inaccuracy in the simulation

predictions for a large value of *dr* could be indicative that these fluid grid sizes are too coarse to capture key features of the fluid flow.

Simulations with *dz* = 2.4 mm all satisfy experimental observation (1) of having the frequency of pressure oscillations approximately equal to that of bubble eruptions, but do not satisfy the experimental observation of a dramatic drop in oscillation frequencies in the H_0 = 50 mm bed. Figure 7 shows that this drop is not predicted because bubbling pattern A is erroneously exhibited in the H_0 = 40 mm bed. Additionally, the ratio of frequencies in Figure 7 (c) and (d) for the simulation with *dz* = 2.4 mm and *dr* = 3.13 mm is even further from experimental results because a bubbling pattern close to pattern B is predicted for the H_0 = 50 mm bed. These simulations give predictions which differ significantly from those seen experimentally, as seen in the time-averaged velocity results; however, in this case the bubbles predicted are fairly axisymmetric.

Simulations with *dz* = 6.0 mm also do not predict the experimental observation of a sudden drop in frequency. In the case of simulations with *dz* = 2.4 mm the drop is not seen because the frequencies in the H_0 = 40 mm bed are too low. Conversely, for simulations with *dz* = 6.0 mm, the frequencies in the bed with H_0 = 50 mm are too high. For simulations with *dz* = 6.0 mm, the frequencies of bubble eruptions and pressure oscillations are too high in the H_0 = 50 mm bed because bubbling pattern B is seen, and thus two bubbles formed consecutively do not interact to decrease the frequency of oscillations. This large difference between experimental and computational results, rooted in differences in predicted bubbling patterns for simulations with *dz* = 6.0 mm, gives a strong example of inaccuracies which can occur when fluid grid sizing is too large. This example is much stronger than that seen in the time-averaged velocity results seen for bed configuration 1.

Simulations with dz = 3.0 mm provided the most complexities in the pressure oscillations and bubble eruption analysis. As seen in Figure 6, only simulations with $dr \geq 5$ mm fully satisfied experimental observation (1), but these simulations did not satisfy observation (2). Simulations with $dr < 5$mm only partially satisfied both observations. Simulations with $dr \geq 5$ mm and dz = 3.0 mm are very similar to those with dz = 2.4 mm: they all predict bubbling pattern A for both bed heights, and thus do not satisfy observation (2), the second key experimental finding. Simulations with $dr < 5$mm exhibit a pattern closer to bubbling pattern B for the H_0 = 40 mm bed, making them closer to simulations with dz = 3.6-4.8 mm from a bubbling pattern perspective. However, the frequency of pressure oscillations is half that of bubble eruption in the H_0 = 40 mm bed, which causes the simulations to not accurately predict the two key experimental findings, as shown in Figure 6. It is unclear which aspect of the flow pattern causes the low frequency of bubble eruption. The complexity in the simulations for dz = 3.0 mm and $dr < 5$ mm is perhaps indicative of simulations which are just barely below the grid spacing necessary to satisfy the assumptions made in the derivation of the volume-averaged fluid equations.

In summary, the pressure oscillations and bubble eruption study support the earlier finding that the optimum fluid grid spacing in the vertical direction is dz = 3.6-4.8 mm, corresponding to 3-4 d_p. The simulations were relatively insensitive to the radial spacing dr, at least within the range 2 d_p to 5 d_p.

3.3 Potential limitations of this study

The criteria for fluid grid sizing emerging from the present work are potentially limited by the facts that (a) only bubbling and slugging fluidized beds were simulated, (b) only Geldart[36] Group D particles with d_p = 1.2 mm were used, (c) an inexact voidage calculation method,

known as the square grid method, was used, and (d) the beds were limited to an internal diameter of 50 mm.

The authors believe that (a) is a serious limitation, and the findings cannot necessarily be generalised to other fluidization regimes or other forms of fluid-particulate flow. Fluidization regime is expected to be a major factor because capturing mesoscopic flow structures on a locally averaged basis is at the heart of appropriate fluid grid sizing, and vastly different mesoscopic flow structures are found in the different fluidization regimes. The mesoscopic structures seen in the simulations conducted here are associated with the flow of bubbles and slugs, which are very different than gas and particle flow in fast fluidization, for example.

The authors do not expect (b) to be an important limitation. The findings are expected to apply to simulations with particles of other sizes and Geldart[36] groupings for two reasons: (1) No assumptions of particle size or grouping are made in the derivation of the volume-averaged fluid equations, and (2) previous work[37] investigating fluid grid sizing found that there was nothing inherently different about simulating fluidization in particles from Groups A, B and D.

The voidage calculation method (c) could be expected to be a limiting factor. Peng *et al.*[5] found that simulations using the point centroid method to calculate voidage became inaccurate at smaller fluid grid sizes than simulations using exact calculations of voidage. This issue is not expected here, because the square grid voidage calculation used here has been shown to be much more accurate and stable than the point centroid method[22]. Additionally, Peng *et al.*[5] found that when simulations using the point centroid method became inaccurate, they violated the conservation of mass of the fluid. By contrast, all of the simulations used in this study were found to satisfy the conservation of mass criterion. Link *et al.*[21] found grid-independent results for grid sizes with side lengths ranging from 2-4 d_p using a void calculation method in which the

particle volume is smoothed over a cube with a side length of 5 d_p. Most current models do not use this amount of smoothing; however, using a method for calculating void fraction with a significant amount of smoothing may allow for slightly smaller grid sizes, and our findings may be limited to void calculation methods with little or no smoothing of particle volume.

The small size of fluidized bed used (d), is expected to be limiting, in that conclusions cannot be drawn as to the limitations in size of fluid grid cells as compared to the size of the bed, as done by Peng *et al.*[5]. Thus, in this work we only provide conclusions as to the size of fluid grid cells relative to the size of particles, though it is worth noting that our system does lie within the range of validity identified by Peng *et al.*[5].

4. Conclusions

The simulations shown in this paper provide a basis on which to set practical limits for the sizing of individual fluid cells in fully 3D DEM-CFD models of bubbling and slugging fluidized beds. The predictions showed non-physical behaviour and substantial differences from experimental results with a fluid grid spacing in the vertical direction (dz) less than three particle diameters (d_p), suggesting that for fluid grids with $dz < 3\ d_p$ the assumptions underlying the validity of the volume averaged fluid equations[3] break down. It was found that simulations with $dz > 4\ d_p$ can provide physically sensible predictions, but miss flow features, whilst if $dz = 3\text{-}4\ d_p$ the predictions closely matched the experimental results. For $dz = 3\text{-}4\ d_p$, the predictions were fairly insensitive to varying fluid grid spacing in the radial direction (dr) from approximately 2 to 5 particle diameters. These criteria for fluid grid sizing are limited to the bubbling and slugging fluidization regimes investigated here; however, the conclusions are not expected to be limited by the gas-solid interaction force correlation, particle size or voidage calculation method used here. Thus, it is recommended that, for fully 3D DEM-CFD simulations of bubbling and

slugging fluidized beds with arbitrary fluid cell geometry, the spacing of the fluid grid be limited to 3-4 particle diameters in the vertical direction, while a range of 2-5 particle diameters, or perhaps an even wider range, is tolerable in the horizontal direction.

Appendix A: Treatment of central axis ($r = 0$) boundary condition

In a fluid grid defined in a cylindrical coordinate system, there is a danger of creating an artificial boundary along the central axis, if the conditions at this axis are not treated carefully. In using the finite volume method on a staggered grid, as done in this DEM-CFD model, many of these issues are avoided; however, the radial fluid velocity still must be interpolated at this point in order to properly discretise some parts of the momentum equation. In order to calculate this radial velocity, a single value for the horizontal velocity vector ($u_x(r = 0, z)$, $u_y(r = 0, z)$) was calculated in rectangular coordinates at the central axis, as done by Takeuchi *et al.*[17] and Fukagata and Kasagi[27]. From this horizontal velocity vector, the radial velocity for each fluid cell in the central annulus ($u_r(r = 0, \theta, z)$) was calculated, according to

$$u_r(r = 0, \theta, z) = u_x(r = 0, z)\cos\theta + u_y(r = 0, z)\sin\theta \qquad \text{(A.1)}$$

The method for calculating the horizontal velocity vector was slightly different from the approaches of Takeuchi *et al.*[17] and Fukagata and Kasagi[27]. Takeuchi *et al.*[17] calculated the horizontal velocity vector using only radial fluid velocities in the central annulus, while Fukagata and Kasagi[27] used only angular fluid velocities. In contrast, both radial and angular velocities were used here. The radial velocities at the $r = dr$ point of each of the inner annulus of fluid cells were combined with angular velocities interpolated at these points to calculate corresponding rectangular velocities, according to

$$u_x(r = dr, \theta, z) = u_r(r = dr, \theta, z)\cos\theta - u_\theta(r = dr, \theta, z)\sin\theta \qquad \text{(A.2)}$$

$$u_y(r = dr, \theta, z) = u_r(r = dr, \theta, z) \sin\theta + u_\theta(r = dr, \theta, z) \cos\theta \qquad \text{(A.3)}$$

The single value for the horizontal velocity vector was then achieved by averaging the horizontal vectors at the radial extreme of the cells in the central annulus:

$$u_x(r = 0, z) = \frac{1}{N_{\theta,1}} \sum_{\theta=1}^{N_{\theta,1}} u_x(r = dr, \theta, z) \qquad \text{(A.4)}$$

$$u_y(r = 0, z) = \frac{1}{N_{\theta,1}} \sum_{\theta=1}^{N_{\theta,1}} u_y(r = dr, \theta, z) \qquad \text{(A.5)}$$

where $N_{\theta,1}$ is the number of grid cells in the angular in the central annulus.

Appendix B: Quantitative differences between experimental results and simulation predictions for frequencies of pressure oscillations and bubble eruptions

Figure B1 shows results for frequencies of pressure oscillations and bubble eruptions in bed configuration 2, corresponding to the result for bed configuration 3 shown in Figure 5. The results shown in Figure B1 for the H_0 = 40 mm bed are initially confusing and seem contradictory to the other results in this study. In Figure B1, the predictions from simulations with *dz* = 2.4 and 6.0 mm match experimental results most closely, while predictions from simulations with *dz* = 3.6 and 4.8 mm are furthest away. In order to understand why this occurs, we must first understand the predictions of bubble formation frequency in the various simulations.

Figure B2 shows the frequencies of bubble formation for bed configurations 2 and 3. For both bed heights, the frequency of bubble formation is approximately equal for simulations with the same fluid grid spacing. The frequencies decrease substantially with increasing *dz*. All of the frequencies predicted are higher than the expected frequency of bubble formation of approximately 5 Hz. This expected frequency of bubble formation is based on the experimental

frequency of bubble eruption of 5 Hz in the H_0 = 40 mm bed and the finding[31] that for short bubbling fluidized beds, the frequency of bubble formation was equal to the frequency of bubble eruption. The reason why all simulations predict bubble formation frequencies higher than the expected value is not fully understood, but it can be attributed in part to inaccuracies in modelling the drag force, as described elsewhere[24].

The frequency of bubble formation predicted by simulations with dz = 2.4 mm are the highest, and thus furthest from the expected value. This demonstrates that these simulations are capturing the physical aspects of the system especially poorly, yet their results for bubble eruption and pressure oscillations frequencies in Figure B1 are just below the experimental values. This shift occurs because bubbling pattern A is erroneously predicted for simulations with dz = 2.4 mm in the H_0 = 40 mm bed. Due to the interaction between two bubbles in this bubbling pattern, the frequencies of bubble eruption and pressure oscillations become half that of bubble formation, causing the predicted bubble formation frequency to be well above the expected value, while the other frequencies are just below the experimental value. The predictions for simulations with dz = 3.0 mm are similar to those from simulation with dz = 2.4 mm with some added complexities, for the same subtle reasons described in Section 3.1.3.

In the simulations with dz = 6.0 mm, the predicted frequencies of bubble formation are closest to the expected value. Since bubbling pattern B is correctly exhibited in these simulations for the H_0 = 40 mm bed, the frequencies of bubble eruption and pressure oscillations are also close to the experimental values in Figure B1. However, this grid spacing does not predict bubbling pattern A in H_0 = 50 mm bed height, and thus the predictions in Figures 5 and 6 do not match experimental results. Thus, while Figure B1 leads to some confusing results for simulations with dz = 2.4, 3.0 and 6.0 mm with comparison to experiments, the fact remains that

these simulations are not properly capturing the underlying physical aspects of fluidization, due to their grid sizing.

The predictions for the frequency of bubble formation for simulations with dz = 3.6 and 4.8 mm is significantly higher than the expected value. Since bubbling pattern B is correctly predicted in the H_0 = 40 mm bed, the frequencies in Figure B1 for this value of dz are also significantly higher than the experimental values. However, Figures 5-8 demonstrate that simulations with dz = 3.6-4.8 mm are most properly predicting the underlying physics of the system, and thus the issue with bubble formation frequency is not as directly related to fluid grid sizing. For all values of dz, the predicted frequency of bubble formation is significantly closer to the expected value with lower values of dr, suggesting that fluid grids with more resolution in the horizontal direction can better model the physics associated with bubble formation.

Acknowledgments:
CMB acknowledges the Gates Cambridge Trust for funding his research.

Notation:

dr	Radial fluid grid spacing
d_p	Particle diameter
dz	Vertical fluid grid spacing
H_0	Settle bed height
$N_{\Theta,1}$	Number of fluid grid cells in the angular direction in the central annulus
U	Superficial velocity
u	Instantaneous fluid velocity
U_{mf}	Minimum fluidization velocity
V_z	Time-averaged vertical particle velocity
x	First horizontal direction in rectangular coordinates
y	Second horizontal direction in rectangular coordinates
z	Vertical direction
Greek letters	
ε	Void fraction

References:

(1) Hoomans, B. P. B.; Kuipers, J. A. M.; Briels, W. J.; Van Swaaij, W. P. M. Discrete Particle Simulation of Bubble and Slug Formation in a Two-Dimensional Gas-Fluidised Bed: A Hard-Sphere Approach. *Chem. Eng. Sci.* **1996**, *51* (1), 99.

(2) Tsuji, Y.; Kawaguchi, T.; Tanaka, T. Discrete Particle Simulation of Two-Dimensional Fluidized Bed. *Powder Technol.* **1993**, *77* (1), 79.
(3) Anderson, T. B.; Jackson, R. Fluid Mechanical Description of Fluidized Beds. *Ind. Eng. Chem. Fundam.* **1967**, *6* (4), 527.
(4) Crowe, C.; Sommerfeld, M.; Tsuji, Y. *Multiphase Flows of Droplets and Particles*, 1st ed.; CRC Press: Boca Raton, FL, 1998.
(5) Peng, Z.; Doroodchi, E.; Luo, C.; Moghtaderi, B. Influence of Void Fraction Calculation on Fidelity of CFD-DEM Simulation of Gas-Solid Bubbling Fluidized Beds. *AIChE J.* **2014**, *60* (6), 2000.
(6) Bokkers, G. A.; van Sint Annaland, M.; Kuipers, J. A. M. Mixing and Segregation in a Bidisperse Gas–solid Fluidised Bed: A Numerical and Experimental Study. *Powder Technol.* **2004**, *140* (3), 176.
(7) Di Renzo, A.; Di Maio, F. P. Homogeneous and Bubbling Fluidization Regimes in DEM–CFD Simulations: Hydrodynamic Stability of Gas and Liquid Fluidized Beds. *Chem. Eng. Sci.* **2007**, *62* (1-2), 116.
(8) He, Y.; Wang, T.; Deen, N.; van Sint Annaland, M.; Kuipers, H.; Wen, D. Discrete Particle Modeling of Granular Temperature Distribution in a Bubbling Fluidized Bed. *Particuology* **2012**, *10* (4), 428.
(9) Liu, D.; Xiao, S.; Chen, X.; Bu, C. Investigation of Solid Mixing Mechanisms in a Bubbling Fluidized Bed Using a DEM-CFD Approach. *Asia-Pac. J. Chem. Eng.* **2012**, *7*, S237.
(10) Müller, C. R.; Holland, D. J.; Sederman, A. J.; Scott, S. A.; Dennis, J. S.; Gladden, L. F. Granular Temperature : Comparison of Magnetic Resonance Measurements with Discrete Element Model Simulations. *Powder Technol.* **2008**, *184*, 241.
(11) Müller, C. R.; Scott, S. A.; Holland, D. J.; Clarke, B. C.; Sederman, A. J.; Dennis, J. S.; Gladden, L. F. Validation of a Discrete Element Model Using Magnetic Resonance Measurements. *Particuology* **2009**, *7* (4), 297.
(12) Tagami, N.; Mujumdar, A.; Horio, M. DEM Simulation of Polydisperse Systems of Particles in a Fluidized Bed. *Particuology* **2009**, *7* (1), 9.
(13) Zeilstra, C.; van der Hoef, M. A.; Kuipers, J. A. M. Simulation of Density Segregation in Vibrated Beds. *Phys. Rev. E* **2008**, *77* (3).
(14) Kawaguchi, T.; Sakamoto, M.; Tanaka, T.; Tsuji, Y. Quasi-Three-Dimensional Numerical Simulation of Spouted Beds in Cylinder. *Powder Technol.* **2000**, *109* (1–3), 3.
(15) Guo, Y.; Wu, C.-Y.; Thornton, C. Modeling Gas-Particle Two-Phase Flows with Complex and Moving Boundaries Using DEM-CFD with an Immersed Boundary Method. *AIChE J.* **2013**, *59* (4), 1075.
(16) Chu, K. W.; Yu, A. B. Numerical Simulation of Complex Particle–fluid Flows. *Powder Technol.* **2008**, *179* (3), 104.
(17) Takeuchi, S.; Wang, S.; Rhodes, M. Discrete Element Simulation of a Flat-Bottomed Spouted Bed in the 3-D Cylindrical Coordinate System. *Chem. Eng. Sci.* **2004**, *59* (17), 3495.
(18) Fries, L.; Antonyuk, S.; Heinrich, S.; Dopfer, D.; Palzer, S. Collision Dynamics in Fluidised Bed Granulators: A DEM-CFD Study. *Chem. Eng. Sci.* **2013**, *86*, 108.
(19) Antonyuk, S.; Heinrich, S.; Smirnova, I. Discrete Element Study of Aerogel Particle Dynamics in a Spouted Bed Apparatus. *Chem. Eng. Technol.* **2012**, *35* (8), 1427.
(20) Chu, K. W.; Yu, A. B. Numerical Simulation of the Gas- Solid Flow in Three-Dimensional Pneumatic Conveying Bends. *Ind. Eng. Chem. Res.* **2008**, *47* (18), 7058.
(21) Link, J. M.; Cuypers, L. A.; Deen, N. G.; Kuipers, J. A. M. Flow Regimes in a Spout–fluid Bed: A Combined Experimental and Simulation Study. *Chem. Eng. Sci.* **2005**, *60* (13), 3425.
(22) Boyce, C. M.; Holland, D. J.; Scott, S. A.; Dennis, J. S. Novel Fluid Grid and Voidage Calculation Techniques for a Discrete Element Model of a 3D Cylindrical Fluidized Bed. *Comput. Chem. Eng.* **2014**, *65*, 18.

(23) Boyce, C. M.; Holland, D. J.; Scott, S. A.; Dennis, J. S. Adapting Data Processing To Compare Model and Experiment Accurately: A Discrete Element Model and Magnetic Resonance Measurements of a 3D Cylindrical Fluidized Bed. *Ind. Eng. Chem. Res.* **2013**, *52* (50), 18085.
(24) Boyce, C. M.; Davidson, J. F.; Holland, D. J.; Scott, S. A.; Dennis, J. S. The Origin of Pressure Oscillations in Slugging Fluidized Beds: Comparison of Experimental Results from Magnetic Resonance Imaging with a Discrete Element Model. *Chem. Eng. Sci.* **2014**, *116*, 611.
(25) Tsuji, Y.; Tanaka, T.; Ishida, T. Lagrangian Numerical Simulation of Plug Flow of Cohesionless Particles in a Horizontal Pipe. *Powder Technol.* **1992**, *71* (3), 239.
(26) Chung, T. J. *Computational Fluid Dynamics*; Cambridge University Press: Cambridge; New York, 2010.
(27) Fukagata, K.; Kasagi, N. Highly Energy-Conservative Finite Difference Method for the Cylindrical Coordinate System. *J. Comput. Phys.* **2002**, *181* (2), 478.
(28) Khawaja, H.; Scott, S.; Virk, M.; Moatamedi, M. Quantitative Analysis of Accuracy of Voidage Computations in CFD-DEM Simulations. *J. Comput. Multiph. Flows* **2012**, *4* (2), 183.
(29) Beetstra, R.; Hoef, M. A. Van Der; Kuipers, J. A. M. Drag Force of Intermediate Reynolds Number Flow Past Mono- and Bidisperse Arrays of Spheres. *AIChE J.* **2007**, *53* (2), 489.
(30) Holland, D. J.; Gladden, L. F.; Müller, C. R.; Dennis, J. S.; Sederman, A. J. Spatially Resolved Measurement of Anisotropic Granular Temperature in Gas-Fluidized Beds. *Powder Technol.* **2008**, *182* (2), 171.
(31) Müller, C. R.; Davidson, J. F.; Dennis, J. S.; Gladden, L. F.; Fennell, P. S.; Hayhurst, A. N.; Mantle, M. D.; Rees, A. C.; Sederman, A. J. Oscillations in Gas-Fluidized Beds: Ultra-Fast Magnetic Resonance Imaging and Pressure Sensor Measurements. *Powder Technol.* **2007**, *177* (2), 87.
(32) Kriebitzsch, S. H. L.; van der Hoef, M. A.; Kuipers, J. A. M. Fully Resolved Simulation of a Gas-Fluidized Bed: A Critical Test of DEM Models. *Chem. Eng. Sci.* **2013**, *91*, 1.
(33) Tran-Cong, S.; Gay, M.; Michaelides, E. E. Drag Coefficients of Irregularly Shaped Particles. *Powder Technol.* **2004**, *139* (1), 21.
(34) Hölzer, A.; Sommerfeld, M. New Simple Correlation Formula for the Drag Coefficient of Non-Spherical Particles. *Powder Technol.* **2008**, *184* (3), 361.
(35) Radl, S.; Sundaresan, S. A Drag Model for Filtered Euler–Lagrange Simulations of Clustered Gas–particle Suspensions. *Chem. Eng. Sci.* **2014**, *117*, 416.
(36) Geldart, D. Types of Fluidization. *Powder Technol.* **1973**, *7*, 285.
(37) Wang, J.; van der Hoef, M. a.; Kuipers, J. a. M. Why the Two-Fluid Model Fails to Predict the Bed Expansion Characteristics of Geldart A Particles in Gas-Fluidized Beds: A Tentative Answer. *Chem. Eng. Sci.* **2009**, *64* (3), 622.

Figures:

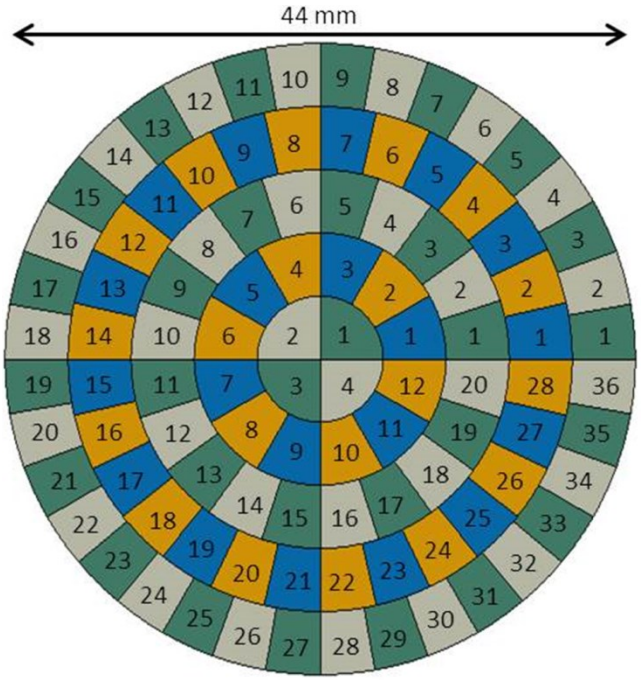

Figure 1. Horizontal cross section of specialised 3D cylindrical CFD grid. There are 5 cells in the radial direction in this grid, each with spacing dr = 4.4 mm. Numbers in each fluid cell serve to count the number of fluid cells in each annulus, in order to note that larger numbers of cells are used in the annuli further from the centre to keep all fluid cells equal in volume.

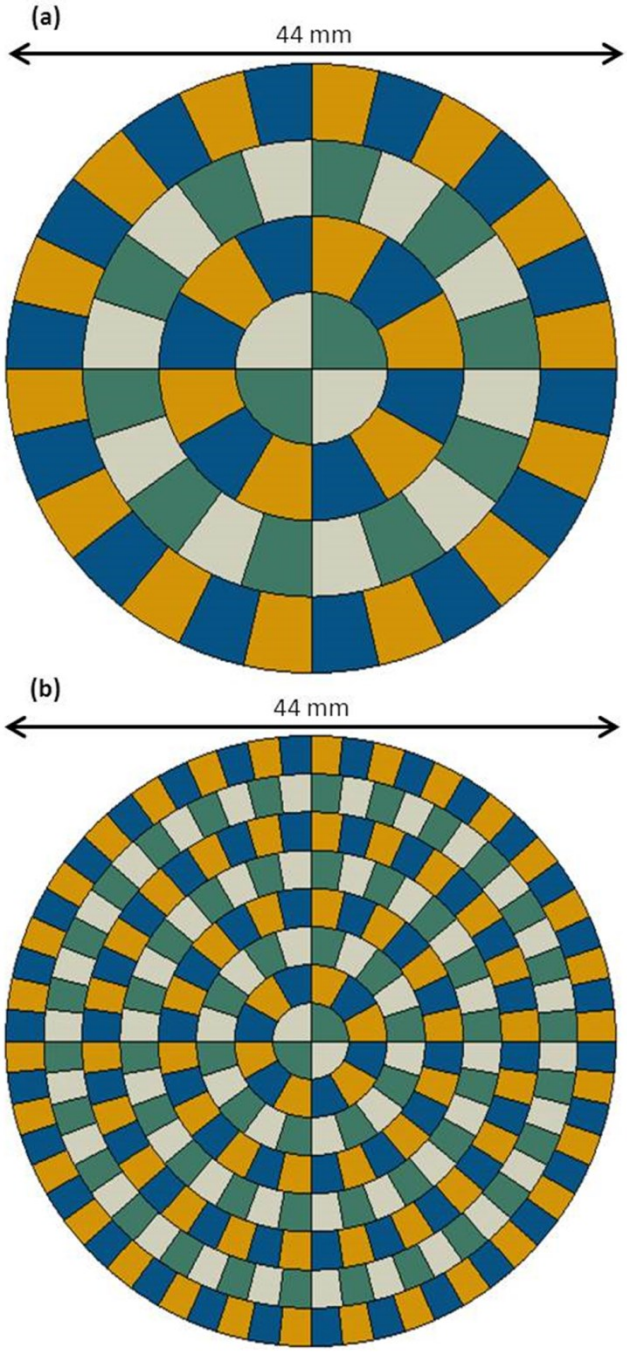

Figure 2. Horizontal cross section of 3D cylindrical fluid grid radial spacing (a) *dr* = 5.5 mm and (b) *dr* = 2.75 mm. Decreasing the grid spacing in the radial direction (*dr*) also decreases spacing in the angular direction.

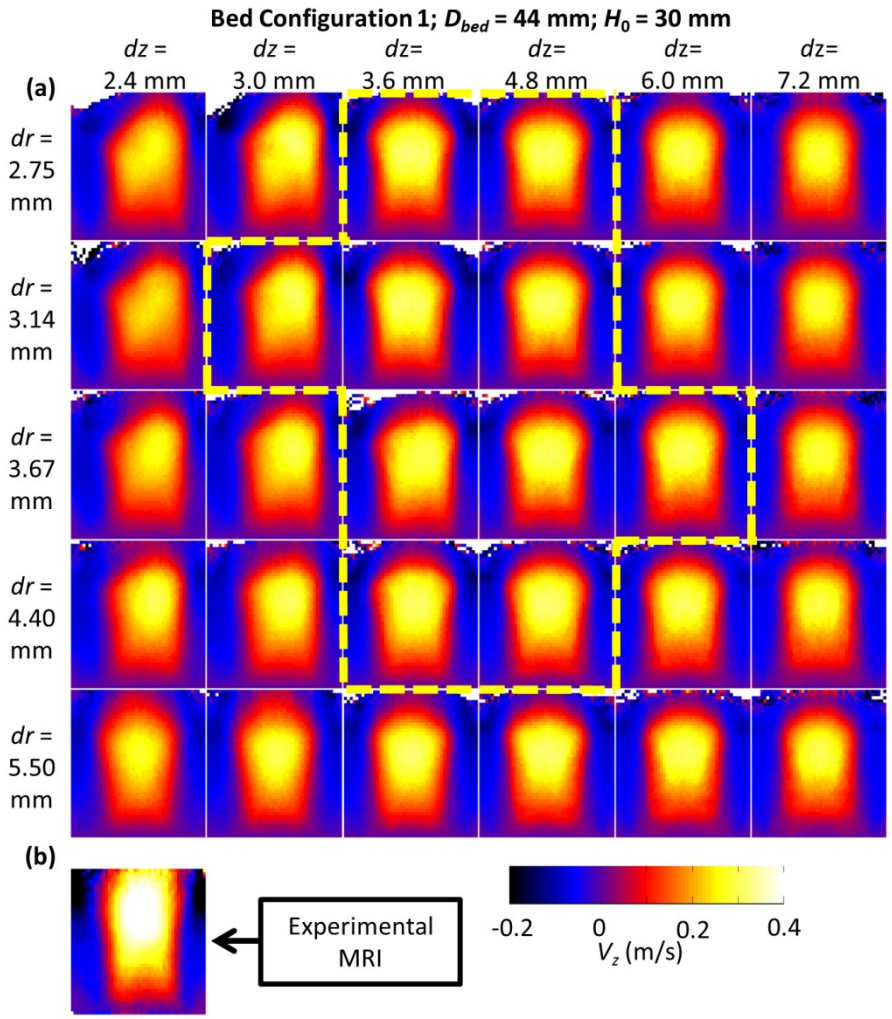

Figure 3. Comparison of time averaged particle velocities in the vertical direction from (a) DEM-CFD simulation predictions with varying sizes of fluid grid cells and (b) experimental results using MRI [30]. For the varying sizes of fluid cells shown in (a), each column is constant in grid sizing in the vertical direction (*dz*) and each row is constant in grid sizing in the radial direction (*dr*). In both (a) and (b) the bed was 44 mm in diameter, filled to an unfluidized bed depth of 30 mm with particles 1.2 mm in diameter and fluidized at $U = 2U_{mf}$. The images show a time-averaged velocity from a 5 mm central slice of the bed in the vertical direction with a field of view of 47 mm (*z*) by 44 mm (*x*), spanning the diameter of the bed and starting vertically just above the distributor, and a resolution of 1.04 mm (*z*) by 0.94 mm (*x*). Profiles within the yellow line have a total squared deviation from experiment, $(\Delta v)_{tot}^2 <$ 0.0080 m/s (see Equation 1). The white corners in the top of some of the images show regions which particles never entered during the simulation.

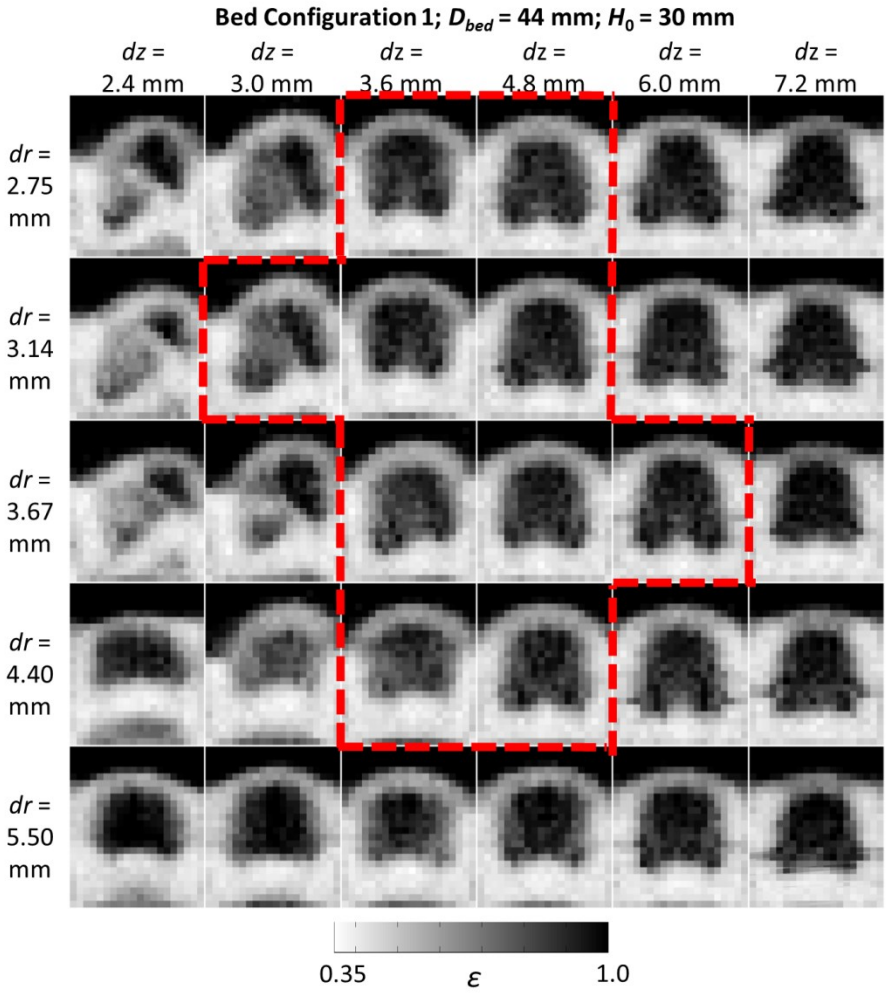

Figure 4. Comparison instantaneous voidage plots of a bubble reaching the bed surface from DEM-CFD simulation predictions with varying sizes of fluid grid cells for bed configuration 1. The images show particle distribution in a 5 mm central slice of the bed in the vertical direction, with dark areas indicating low density of particles and light areas indicating high density of particles. Each column of images is constant in grid sizing in the vertical direction (*dz*) and each row is constant in grid sizing in the radial direction (*dr*). The images have a field of view of 48.4 mm (*z*) by 44.0 mm (*x*), spanning the diameter of the bed and starting vertically just above the distributor, and a resolution of 2.2 mm (*z*) by 2.2 mm (*x*). Profiles within the red line come from a simulation which produced a time-averaged velocity profile with a total squared deviation from experiment, $(\Delta v)_{tot}^2 < 0.0080$ m/s (see Equation 1).

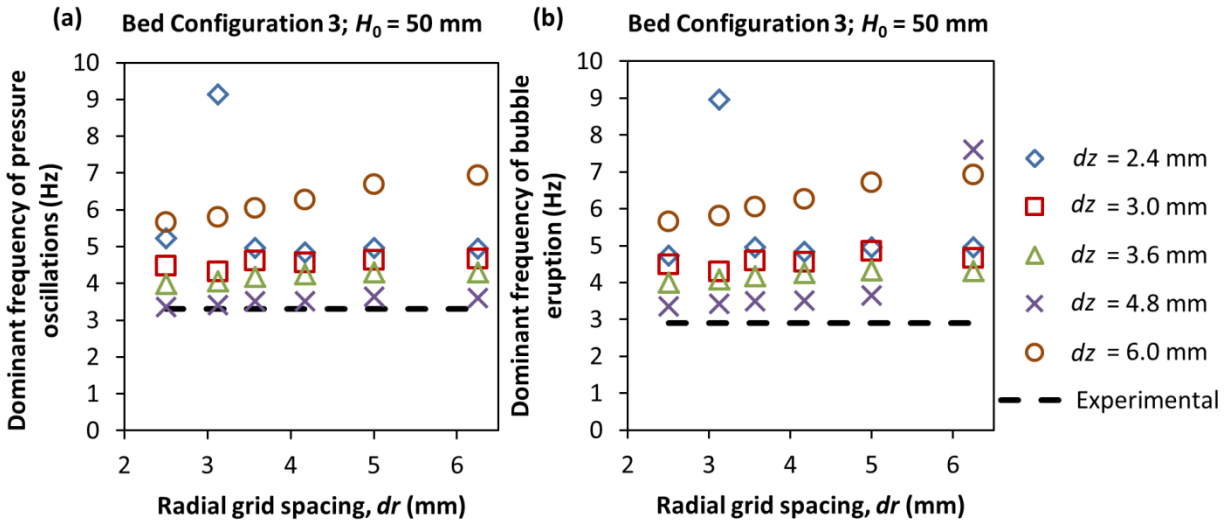

Figure 5. Effects of fluid grid size on DEM-CFD predictions of frequencies of (a) pressure oscillations 10 mm above the distributor and (b) bubble eruption at the bed surface as compared to experimental results [31] for bed configuration 3. Bed diameter: 50 mm; settled bed height: 50 mm; particle diameter: 1.2 mm; U/U_{mf} = 1.88.

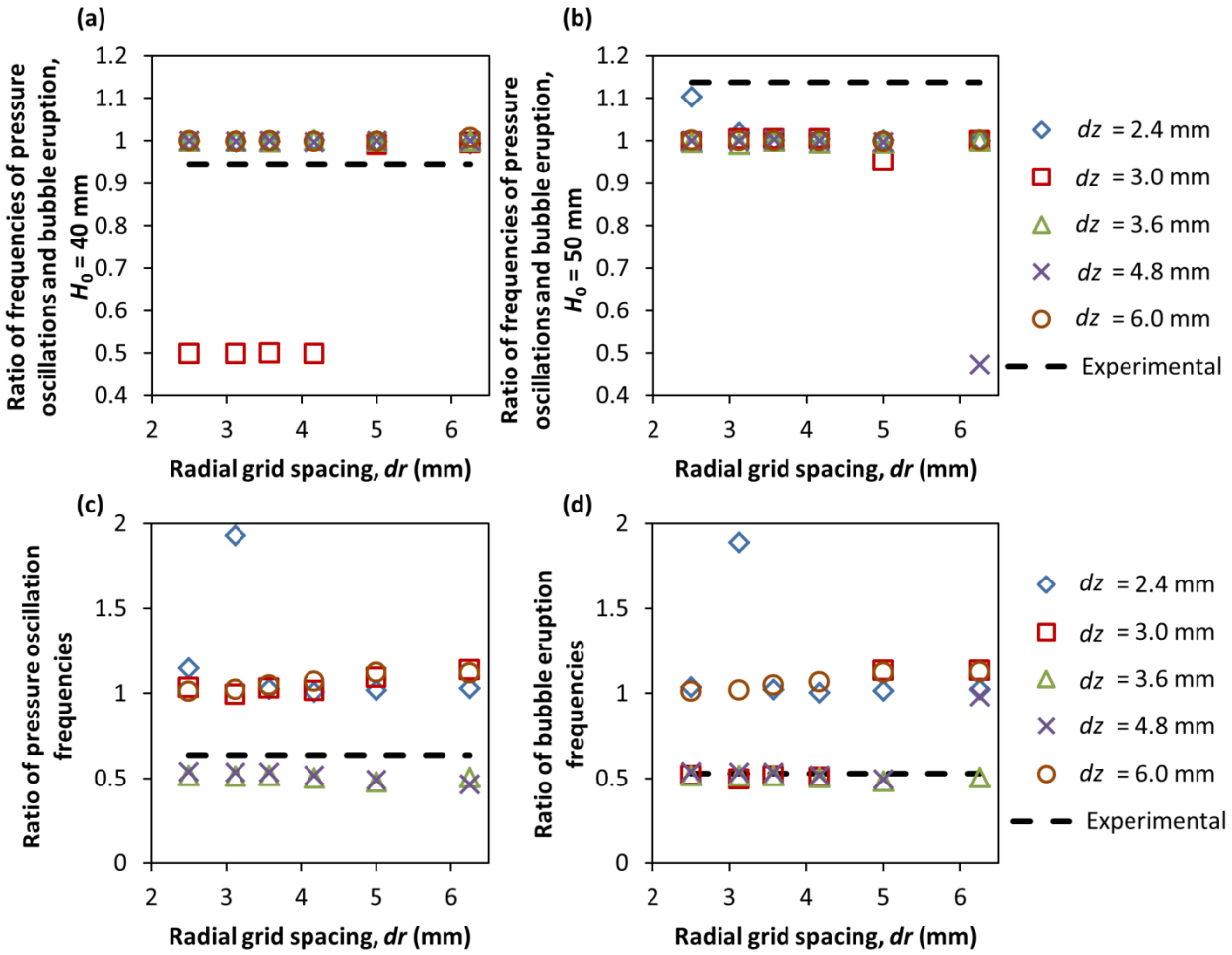

Figure 6. Effects of fluid grid sizing on DEM-CFD predictions of frequencies of pressure oscillations 10 mm above the distributor and bubble eruption at the bed surface for different settled bed heights as compared to experimental results [31]. The ratio of the frequency of pressure oscillations to that of bubble eruptions is shown in (a) and (b) for 40 and 50 mm tall beds, respectively. The ratio of frequencies of pressure oscillations between the 50 and 40 mm tall beds is shown in (c), while the corresponding ratio for bubble eruptions is shown in (d). Bed diameter: 50 mm; particle diameter: 1.2 mm; U/U_{mf} = 1.88.

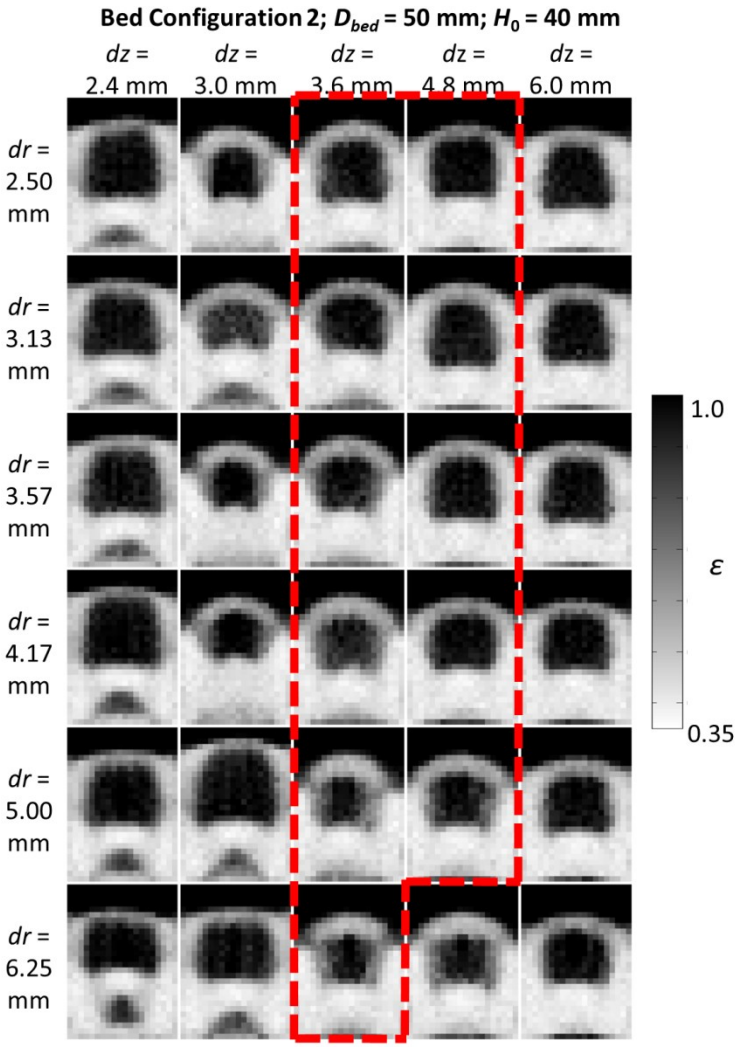

Figure 7. Comparison instantaneous voidage plots of a bubble reaching the bed surface from DEM-CFD simulation predictions with varying sizes of fluid grid cells for bed configuration 2. The images show particle distribution in a 5 mm central slice of the bed in the vertical direction, with dark areas indicating low density of particles and light areas indicating high density of particles. Each column of images is constant in grid sizing in the vertical direction (*dz*) and each row is constant in grid sizing in the radial direction (*dr*). The images have a field of view of 70 mm (*z*) by 50 mm (*x*), spanning the diameter of the bed and starting vertically just above the distributor, and a resolution of 2.5 mm (*z*) by 2.5 mm (*x*). Profiles within the red line come from a fluid grid size which approximately matched experimental data for all 4 cases shown in Figure 7.

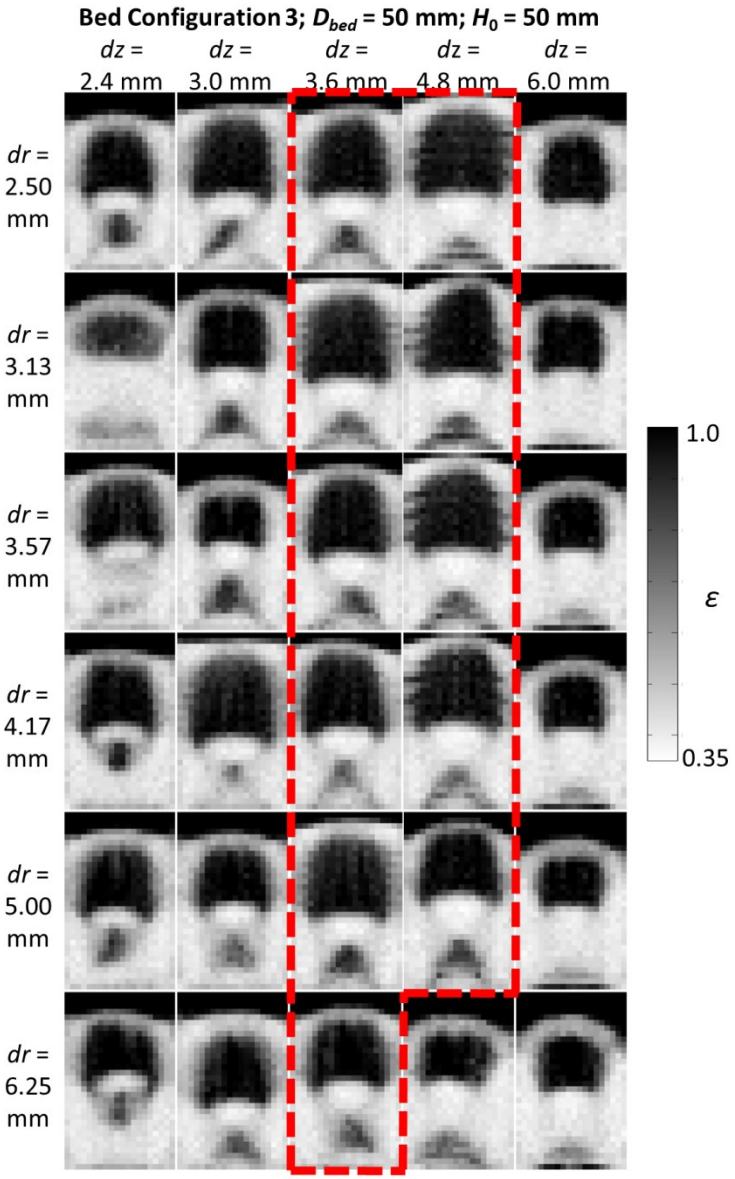

Figure 8. Comparison instantaneous voidage plots of a bubble reaching the bed surface from DEM-CFD simulation predictions with varying sizes of fluid grid cells for bed configuration 3. The images show particle distribution in a 5 mm central slice of the bed in the vertical direction, with dark areas indicating low density of particles and light areas indicating high density of particles. Each column of images is constant in grid sizing in the vertical direction (*dz*) and each row is constant in grid sizing in the radial direction (*dr*). The images have a field of view of 80 mm (*z*) by 50 mm (*x*), spanning the diameter of the bed and starting vertically just above the distributor, and a resolution of 2.5 mm (*z*) by 2.5 mm (*x*). Profiles within the red line come from a fluid grid size which approximately matched experimental data for all 4 cases shown in Figure 7.

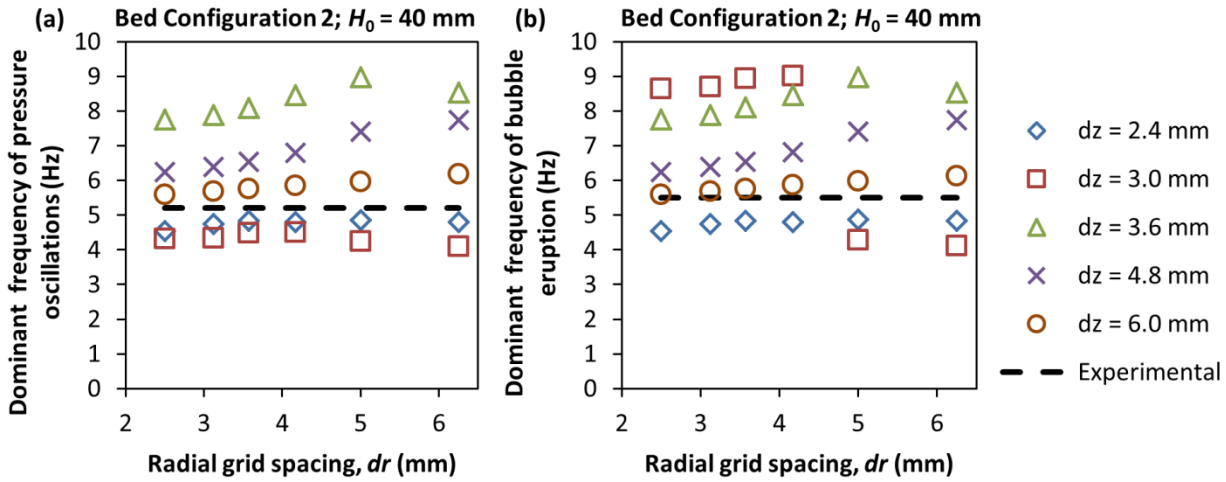

Figure B1. Effects of fluid grid size on DEM-CFD predictions of frequencies of (a) pressure oscillations 10 mm above the distributor and (b) bubble eruption at the bed surface as compared to experimental results[31] for bed configuration 2. Bed diameter: 50 mm; settled bed height: 40 mm; particle diameter: 1.2 mm; U/U_{mf} = 1.88.

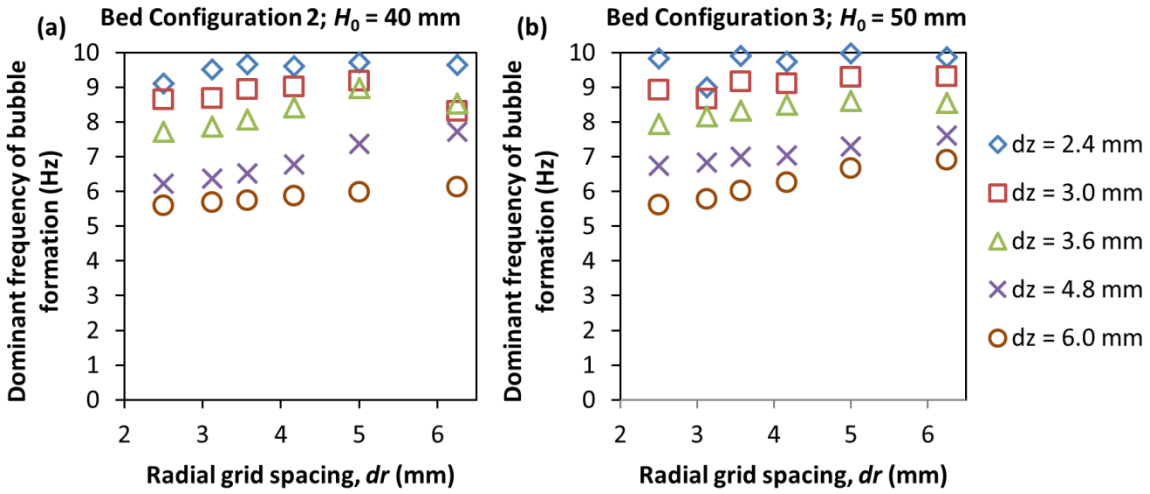

Figure B2. Effects of fluid grid size on DEM-CFD predictions of frequencies of bubble formation at the distributor for (a) bed configuration 2 and (b) bed configuration 3.

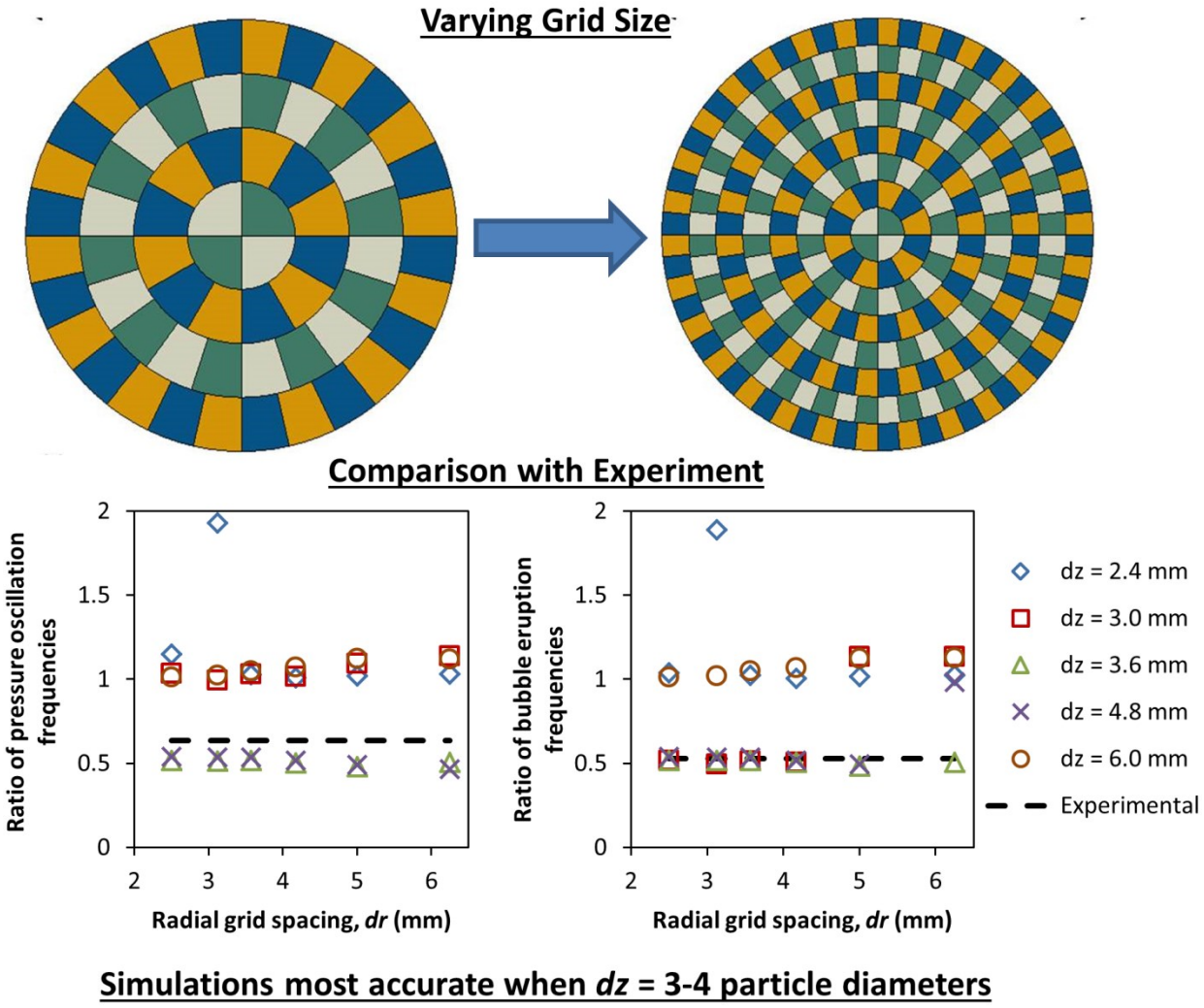

Table of Contents Figure

Tables:

Table 1. Parameters used for DEM-CFD simulations in bed configuration 1

Parameter	Value	
	Config. 1	**Config. 2 and 3**
Fluid Grid Radial Spacing (*dr*)	2.75 mm 3.14 mm 3.67 mm 4.40 mm 5.50 mm	2.50 mm 3.13 mm 3.57 mm 4.17 mm 5.00 mm 6.25 mm
Fluid Grid Vertical Spacing (*dz)*	2.4 mm 3.0 mm 3.6 mm 4.8 mm 6.0 mm 7.2 mm	2.4 mm 3.0 mm 3.6 mm 4.8 mm 6.0 mm
Diameter of Bed	44 mm	50 mm
Diameter of Particles	1.2 mm	1.2 mm
Density of Particles	900 kg/m^3	960 kg/m^3
Geldart Group	D	
Coefficient of Sliding Friction	0.1	
Young's Modulus	1.2×10^8 Pa	
Poisson's Ratio	0.33	
Normal Damping Coefficient	0.02	
Tangential Damping Coefficient	0.0001	
Time Step (fluid and particles)	1.25×10^{-6} s	

Table 2. Deviation from experimental results (m^2/s^2) of time averaged velocity predictions of simulations with various grid sizes. The deviation is the sum of the squared-difference of each pixel up to 42 mm above the distributor, according to Equation 1.

		dz (mm)					
		2.4	3.0	3.6	4.8	6.0	7.2
dr (mm)	2.75	0.0106	0.0086	0.0063	0.0074	0.0082	0.0098
	3.14	0.0137	0.0071	0.0078	0.0072	0.0086	0.0098
	3.67	0.0122	0.0097	0.0071	0.0076	0.0069	0.0097
	4.40	0.0094	0.0082	0.0070	0.0074	0.0084	0.0097
	5.50	0.0090	0.0081	0.0084	0.0083	0.0086	0.0100

Table 3. Quantification of the upward moving velocity profile: average velocity (m/s) of the 216 (highest 10%) pixels with the highest time-averaged vertical particle velocity for simulations with various grid sizes. The corresponding value for the MRI experimental study was 0.410 m/s.

		dz (mm)					
		2.4	3.0	3.6	4.8	6.0	7.2
dr (mm)	2.75	0.236	0.271	0.288	0.278	0.267	0.250
	3.14	0.220	0.266	0.287	0.280	0.268	0.251
	3.67	0.237	0.262	0.275	0.279	0.275	0.254
	4.40	0.263	0.270	0.283	0.286	0.274	0.260
	5.50	0.243	0.264	0.283	0.287	0.278	0.265

Table 4. Quantification of the downward moving velocity profile: average velocity (m/s) of the 216 (highest 10%) pixels with the lowest time-averaged vertical particle velocity for simulations with various grid sizes. The corresponding value for the MRI experimental study was -0.180 m/s.

		dz (mm)					
		2.4	3.0	3.6	4.8	6.0	7.2
dr (mm)	2.75	-0.087	-0.114	-0.105	-0.092	-0.083	-0.075
	3.14	-0.103	-0.096	-0.104	-0.091	-0.081	-0.074
	3.67	-0.087	-0.088	-0.105	-0.092	-0.091	-0.084
	4.40	-0.087	-0.089	-0.107	-0.096	-0.084	-0.085
	5.50	-0.085	-0.091	-0.099	-0.093	-0.083	-0.081